Synergistic polarity interaction and structural reconstruction in Bi_2MoO_6/C_3N_4 heterojunction for enhancing piezo-photocatalytic nitrogen oxidation to nitric acid

Xiaoxu Deng [a], Peng Chen [c], Ruirui Cui [a], Xingyong Gong [a], Xucheng Li [a], Xu Wang [a], Chaoyong Deng [a,b,*]

[a] Key Laboratory of Electronic Composites Materials of Guizhou Province, College of Big Data and Information Engineering, Guizhou University, Guiyang, Guizhou 550025, China
[b] School of Electronics and Information Engineering, Guiyang University, Guiyang, Guizhou 550005, China
[c] Key Laboratory of Green Chemical and Clean Energy Technology of Guizhou Provincial, School of Chemistry and Chemical Engineering, Guizhou University, Guiyang, Guizhou 550025, China

ARTICLE INFO

ABSTRACT

Constructing heterojunctions has emerged as a widely embraced strategy for augmenting piezo-photocatalytic activities. However, the synergistic pressure response, the construction of charge transfer, polar direction sites and active site are often left in the basket. Here, the carboxylated C_3N_4 and Bi_2MoO_6 S-scheme heterostructure was elaborately designed for piezo-photocatalytic nitrogen oxidation towards nitric acid. Extensive research evidence proves that Bi-COOH interaction between Bi_2MoO_6 and g-C_3N_4 leads to the occurrence of polarity interaction and structural reconstruction. Those initiatives facilitate the efficient distribution of charges and acts as a pathway for carrier migration, thereby promoting charge transfer and the large intrinsic dipole moment. Furthermore, the combination of polarity interaction and structural reconstruction strengthens N_2 polarization and electron transfer, facilitating the breaking of N≡N bonds and reducing activation energy. Consequently, the optimal BCO-3 catalyst revealed outstanding nitric acid production rates of 5930 μg g^{-1} h^{-1} under the stimulation of ultrasonic and light illumination, which is 3.66 times higher than that of C_3N_4-Bi_2MoO_6 heterostructure and superiors to various piezo-photocatalysts. Our research endeavors present promising prospects for the design of advanced catalysts and contribute to a profound comprehension of molecular activation processes in heterojunction.

1. Introduction

Nitrate is considered to be one of the most important basic raw material for the fertilizers, explosives, pharmaceuticals, dyes and emulsifiers field [1–3]. Presently, the industrial nitrate production is derived from a two-step procedure involving Haber-Bosch process and Ostwald process [4,5], resulting in huge energy consumption and greenhouse effect. Recently, directly photocatalytic nitrogen oxidation to generate nitrate using O_2 as oxidizing agent (PNO) represents a sustainable and alternative strategy, because of the merit of simple reaction systems, gentle reaction conditions, eco-friendliness, and affordability [6]. Considering the stronger N≡N triple bonds energy (941 kJ mol^{-1}),

the symmetry forbidden of molecule orbital mechanism, and rapid carrier recombination rate in PNO [7–9], resulting in photocatalytic efficiency is not satisfactory. Recently, piezo-catalysis cooperated photocatalysis attracts unprecedented research enthusiasm for enhancing photocatalytic performance [10,11]. The presence of external stress can generate a significant polarization field and polarized charges, thereby facilitating directional charge transfer, as well as the adsorption and activation of reactant molecules [12,13]. Therefore, it is expected that the combination of piezo-catalysis and photocatalysis will achieve a breakthrough in nitrogen oxidation for nitrate generation.

Currently, the most prominent research area in piezo-photocatalysis is focused on developing highly efficient catalysts. Bismuth molybdate

---

* Corresponding author at: Key Laboratory of Electronic Composites Materials of Guizhou Province, College of Big Data and Information Engineering, Guizhou University, Guiyang, Guizhou 550025, China.
E-mail address: cydeng@gzu.edu.cn (C. Deng).

(Bi_2MoO_6, BMO), possessing a distinctive Aurivillius family structure and demonstrating favorable oxidizing capacity, has been reported as a two-dimensional ferroelectric material capable of effectively harnessing various forms of natural mechanical and solar energy [14–16]. These advantages have led to significant advancements in the piezo-photocatalytic fields of pollutant degradation and nitrogen fixation, which is expected to effectively activate and adsorb nitrogen [17, 18]. However, the piezo-photocatalytic performance can be significantly hindered by factors such as a diminished charge shielding effect, limited capture areas for mechanical energy, reduced piezoelectric polarization, and insufficient catalytic active sites [19]. To address these dilemmas, various approaches including morphological control, metal loading, and vacancy engineering have been proposed [20–23]. Constructing heterojunctions, which is a popular strategy, holds great potential for enhancing piezo-photocatalytic activities [24–28]. Due to the suitable band structure and facile synthesis, excellent nitrogen adsorption performance, and favorable piezoelectricity, $g-C_3N_4$ has been widely utilized in water splitting, CO_2 reduction, selective organic transformation and nitrogen fixation [29–31], which has the potential to be an excellent candidate for constructing heterojunctions with Bi_2MoO_6 and effectively activating nitrogen. However, such as the traditional photocatalytic design ideas, those strategies are mainly concentrated on tight heterojunction, interface charge transfer. The synergistic pressure response, construction of charge transfer, polar direction sites and active site are often left in the basket. In addition, the correct tactic of building heterogeneous structures remains questionable.

Herein, we designed the carboxylated C_3N_4 (CNO) and Bi_2MoO_6 to form a highly efficient S-scheme heterostructure for piezo-photocatalytic N_2 oxidation to NO_3^-. The optimal carboxylated C_3N_4-Bi_2MoO_6 (BCO) catalyst revealed outstanding nitric acid production rates of 5930 $\mu g\ g^{-1}\ h^{-1}$ under the stimulation of ultrasonic and light illumination, this rate is 4.86 and 3.66 times higher than that of BMO and BBC and superiors to various piezo-photocatalysts. Fortunately, it was found that Bi-COOH interaction between Bi_2MoO_6 and $g-C_3N_4$ leads to the occurrence of polarity interaction and structural reconstruction. On the one hand, it facilitates the efficient distribution of charges and acts as a pathway for carrier migration, thereby promoting charge transfer and the large intrinsic dipole moment. Moreover, the combination of polarity interaction and structural reconstruction strengthens N_2 polarization and electron transfer, ultimately facilitating the breaking of N≡N bonds with reduced activation energy.

2. Experimental section

2.1. Preparation of Bi_2MoO_6 (BMO) nanosheet

In general, a mixture of $Na_2MoO_4\cdot2\ H_2O$ (0.242 g), $Bi(NO_3)_3\cdot5\ H_2O$ (0.970 g) and cetyltrimethylammonium bromide (CTAB) (0.3 g) was prepared in 80 mL of H_2O and stirred for 30 minutes. The solution obtained was subsequently transferred to 100 mL of Teflon lined autoclave and heated at 180 °C for 16 hours. Finally, the product was obtained through washing, filtration and drying procedures as per standard protocol.

2.2. Preparation of $g-C_3N_4$ (CN) nanosheet

To obtain the $g-C_3N_4$ nanosheet, a total of 6 g of melamine powder was subjected to controlled heating in a covered alumina crucible. The temperature was gradually increased from 20 °C/min until reaching 520 °C for a duration of 2 hours. Subsequently, the temperature was further raised at the same rate until reaching 540 °C for an additional 2 hours.

2.3. Preparation of $g-C_3N_4$ acidified (CNO) nanosheet

In general, a solution is prepared by dissolving 1 g of CN powder in 30 mL concentrated sulfuric acid. The mixture is then stirred at a temperature of 60 °C for one hour and subsequently cooled slowly to 0 °C using an ice bath. Within a span of 20 minutes, the mixture is gradually combined with 1.2 g of potassium permanganate, followed by gentle heating until reaching a temperature of 30 °C while being agitated. Subsequently, a moderate amount of deionized water (200 mL) is added dropwise to the suspension. It should be ensured that during the initial five-minute period, the suspension temperature remains below 30 °C before introducing small amounts of a milky H_2O_2 aqueous solution (5%) into the mixture. Finally, strain, wash thoroughly and dry to obtain CNO.

2.4. Preparation of Bi_2MoO_6 and CNO heterojunction (BCO-x)

Typically, a solution was prepared by dispersing 0.5 g of Bi_2MoO_6 and 0.1 g of CNO separately in 30 mL of deionized water under stirring for 3 hours. Subsequently, the two components were mixed thoroughly and subjected to ultrasonication for 2 hours. The solution obtained was subsequently transferred into a Teflon-lined autoclave with a capacity of 100 mL. It was then subjected to heating at a temperature of 180 °C for a period lasting 6 hours. Finally, the product was obtained through washing, filtration and drying processes, yielding BCO-1 as the final product. Additionally, different mass ratios between Bi_2MoO_6 and CNO were prepared using the same methods described above but with varying amounts of CNO (0.2 g, 0.3 g, 0.4 g and 0.5 g), resulting in BCO-2, BCO-3, BCO-4 and BCO-5 respectively.

2.5. Preparation of Bi_2MoO_6 and $g-C_3N_4$ (CN) heterojunction (BBC)

Typically, 0.5 g of Bi_2MoO_6 and 0.5 g of CN were separately dispersed in 30 milliliters of deionized water with continuous stirring for a duration of 3 hours. Subsequently, the two components were thoroughly mixed and subjected to ultrasonication for a period of 2 hours. The resulting solution was then transferred into a Teflon-lined autoclave with a capacity of 100 milliliters, followed by heating at a temperature of 180 °C for a total duration of 6 hours. Finally, the product was obtained through successive procedures involving washing, filtration and drying.

3. Results and discussion

3.1. Analysis of material structures

The morphology of as-prepared samples can be explored by using scanning electron microscopy (SEM), transmission electron microscopy (TEM) and atomic force microscope (AFM). As exhibited in Fig. 1a and S1 (Supporting Information, SI), all the prepared samples have lamellar morphology with irregular rectangular structure. From AFM images (Fig. S2, SI), the BMO, CNO, BBC and BCO-3 exhibit a nanosheet-like morphology with thicknesses measured at 7.69, 11.37, 25.30 and 23.25 nm, respectively. From Fig. S3 (SI), the measured specific surface area of BCO-3 was approximately 32.38 $m^2 g^{-1}$, which are larger than that of BMO (8.22 $m^2\ g^{-1}$), CNO (12.67 $m^2\ g^{-1}$) and BBC (15.62 $m^2\ g^{-1}$), suggesting the lamellar structure facilitates exposure of the active site for molecular activation. Additionally, the high-resolution transmission electron microscopy (HRTEM) image of BCO-3 displayed a lattice spacing measuring 0.27 nm, which corresponds to the (002) crystallographic plane of Bi_2MoO_6 [32]. Furthermore, the compact interface between porous and amorphous structures was identified as C_3N_4 (Fig. 1c). This compact interface is contributed to facilitates charge separation and catalytic activities. The corresponding EDS mapping image exhibited a homodisperse of Mo, O, Bi, N and C, suggesting the BCO-3 heterojunction was successfully prepared.

The detailed phase and crystalline structure of the fabricated catalysts were analyzed by X-ray diffraction (XRD). As depicted in Fig. S4 (SI), although BBC and BCO-x exhibit characteristic peaks of Bi_2MoO_6,
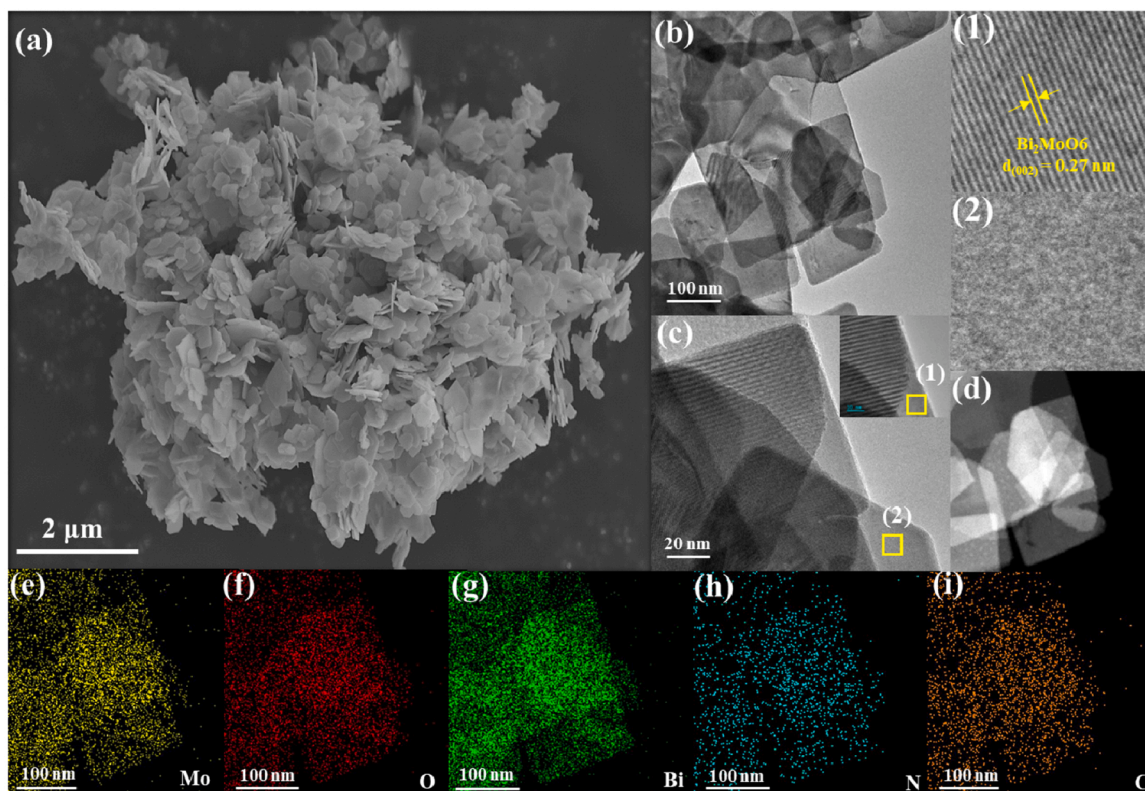
Fig. 1. (a) SEM image, (b-d) TEM and (e-i) the corresponding mapping images of BCO-3.

the distinctive peaks of g-C$_3$N$_4$ cannot be detected, which can be attributed to the overlapping of the (131) plane of Bi$_2$MoO$_6$ with the (002) plane of g-C$_3$N$_4$ [33]. Interestingly, the (131) crystal planes of BCO-x exhibit a higher angular shift compared to the diffraction pattern of Bi$_2$MoO$_6$, indicating a reduction in layer spacing and suggesting intimate interfacial contact between Bi$_2$MoO$_6$ and g-C$_3$N$_4$. To further confirm the structure of C$_3$N$_4$, the Fourier transform infrared (FT-IR) has been investigated. As shown in Fig. 2a, the stretching vibrations modes of the heptazine heterocyclic ring (C$_6$N$_7$) units are located at the range 1650–1200 cm^{-1}, suggesting the successful preparation of Bi$_2$MoO$_6$ and g-C$_3$N$_4$ heterojunction. Notably, a peak at 1705 cm^{-1}, belonging to the COOH bond in CNO [34], demonstrating the BCO-3 consist of BMO and CNO. Notably, the characteristic FT-IR bands at 1455 cm^{-1} assigned to the COO$^-$ groups in BCO-3 [35]. Additionally, the IR stretching vibration of CNO exhibited a higher wavenumber in BCO-3 compared to CNO, indicating the enhanced electron cloud density observed at the interface between BCO-3. This can be attributed to the robust interfacial interactions of CNO and BMO, which facilitate efficient charge transfer at the interface. Meanwhile, the characteristic Raman peaks at 144, 289, 352, 401 and 709, 789, 841 cm^{-1} correspond to the lattice mode of Bi^{3+} and the E$_g$ bending of Bi–O bonds, E$_u$ symmetric bending and stretching modes of MoO$_6$ octahedrons band (Fig. S5, SI) [36]. Notably, the peak at 144 and 289 cm^{-1} exhibited a redshift towards lower wavenumbers, accompanied by an enhancement in the intensity of its characteristic peak, suggesting the Bi–O bond underwent a significantly structural reconstruction.

X-ray photoelectron spectroscopy (XPS) analysis was employed to reveal the electronic structure. As displayed in Fig. 2b–e, BCO-3 have two peaks at 158.69 and 164.00 eV are belonged to Bi 4f$_{7/2}$ and Bi 4f$_{5/2}$ of Bi^{3+}, respectively [37]. For Mo 3d spectrum, the peaks of BCO-3 at 231.75 and 234.88 eV are related to Mo 3d$_{5/2}$ and Mo 3d$_{3/2}$ of Mo^{6+} [38]. Besides, the peaks at 284.68, 286.06, 288.03 and 289.56 eV are corresponded to C–C, C–O, N–C＝N and COOH bonds [39], respectively. In Fig. 2d, The N 1s spectrum with high resolution exhibited three

distinct peaks at 398.44, 399.98 and 401.55 eV, corresponding to the presence of C–N＝C bonds, N–(C)$_3$ bonds and C–N–H bonds [40], respectively. Significantly, a slight shift towards higher binding energy is observed in comparison to C$_3$N$_4$, which can be attributed to the electron-withdraw effects of C＝O and COOH units. Fig. S6 (SI) illustrates the high-resolution O 1s spectrum, BCO-3 exhibits three distinct peaks located at 530.48, 531.18, 531.90, and 532.52 and 533.24 eV, which can be attributed to metal-oxygen bonds, O–C＝O bonds, defective oxygen species, adsorbed oxygen, and C＝O bonds [41,42], respectively. The lattice imperfection in BCO-3 is further explored by the electron paramagnetic resonance (EPR) spectroscopy. Fig. S7 (SI) shown that BBC and BCO-3 possess the large peaks at the g = 2.003, which are assigned to O vacancies [43,44]. Additionally, compared to the XPS peaks observed for CNO and BMO, a noticeable shift in the BCO-3 composite suggests an evident interaction between Bi$_2$MoO$_6$ and g-C$_3$N$_4$. In addition, the Bi 4 f and Mo 3d spectrum shift to the lower energy compared to the BBC, suggesting the electron drawing effect is probably achieved through the interaction of Bi-COOH between Bi$_2$MoO$_6$ and g-C$_3$N$_4$, which would accelerate local polarization interaction and thus promote the charge transfer.

To investigate the coordination environment at the interface, X-ray absorption fine structure spectroscopy (EXAFS) was employed. In Fig. 2f, it can be observed that the energy level of Bi in BCO-3 is shifted towards a lower value compared to that of BMO. This observation further supports the presence of charge polarization in the heterojunction and suggests an electron transfer from Bi to COOH. Quantitative structural parameters of Bi in the Bi-COOH catalyst were obtained through a least-squares EXAFS curve fitting analysis. Bi−Bi coordination peak at 3.5 Å and the Bi−O coordination peak at 1.6 Å [45]. Significantly, in comparison to the BMO, the intensity and length of Bi−O in the EXAFS spectra is more pronounced (Fig. 2g), suggesting there is an increased coordination number of Bi−O in the BCO-3, which may be ascribed to the presence of coordinated Bi-COOH bonds. On the other hand, the presence of coordinated Bi-COOH bonds induce a structural
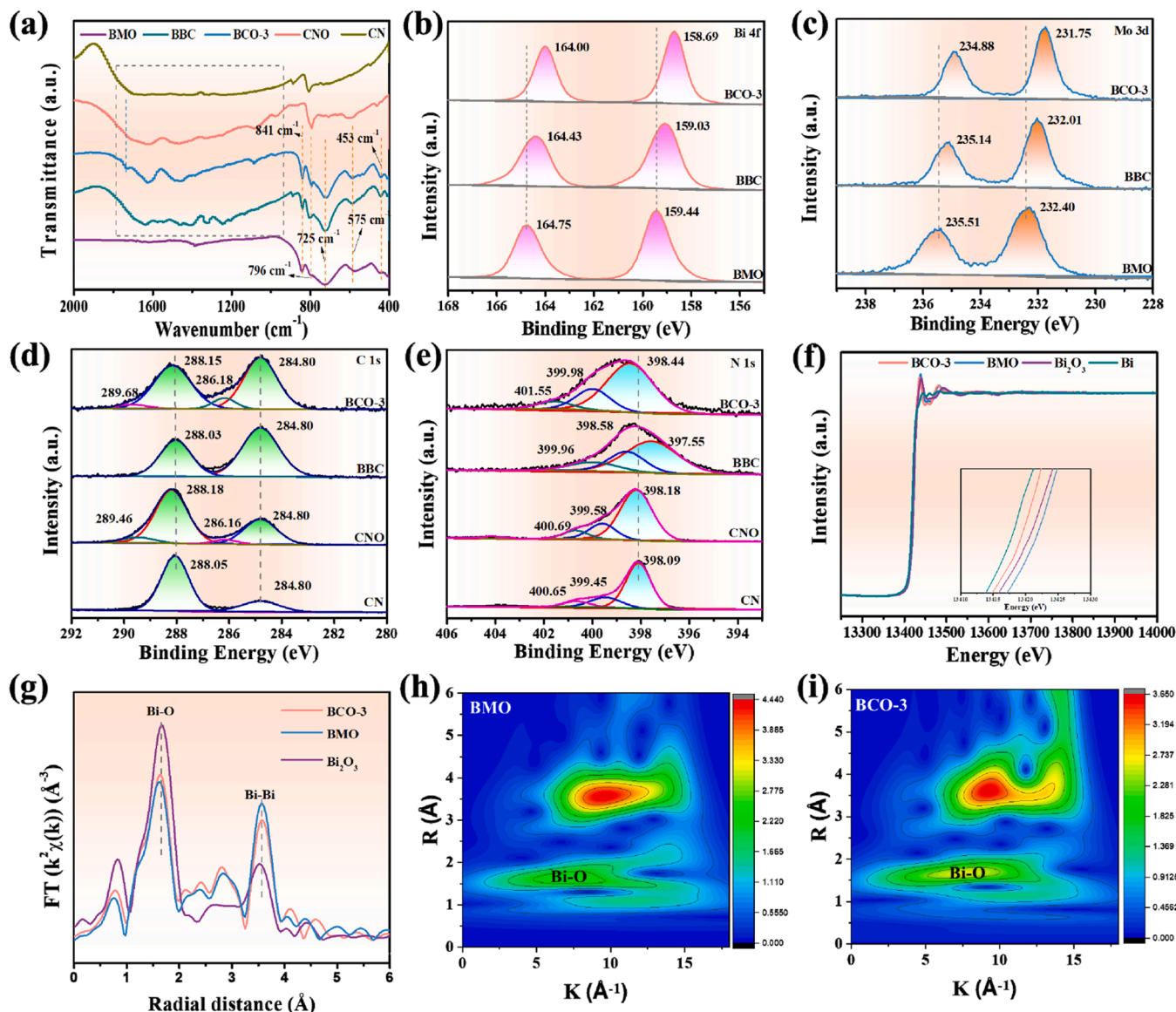
Fig. 2. (a) FT-IR spectra of as-obtained samples. XPS spectra of (b) Bi 4 f, (c) Mo 3d, (d) C 1 s and (e) N 1 s for prepared samples. (f) The normalized XANES spectra of Bi in Bi, Bi_2O_3, BMO and BCO-3. (g) Fourier-transformed Bi K-edge EXAFS in Bi_2O_3, BMO and BCO-3. Wavelet transformed EXAFS of (h) BMO and (i) BCO-3.

reconstruction for enhancing the exposure of the active site. Moreover, the bond length of 4.6 Å for the BCO-3, suggesting that isolated Bi atoms are coordinated by COOH atoms [46,47]. Besides, The Bi-COOH bond is further supported by the intensity maxima observed at approximately 14.3 $Å^{-1}$ in the wavelet transform (WT) contour plots of the BCO-3 (Fig. 2h–i).

3.2. Analysis of piezo-photocatalytic carrier migration

It is widely acknowledged that the migration capacity of a material's carriers can be effectively regulated through the combined effects of its piezoelectric and photoelectrochemical properties [48]. Therefore, it is necessary to consider these inherent characteristics. Firstly, the UV–vis absorption spectra were utilized to measure the property of light absorption. As illustrated in Fig. S8 (SI), BMO, BBC and BCO-x exhibit capability for absorbing visible light with an absorption edge close to 480 nm, while CNO has an absorption edge at approximately 420 nm. Accordingly, the optical bandgaps of BMO, CNO and CN were determined to be 2.68, 3.02 and 2.77 eV, respectively. Moreover, the XPS valence band spectra revealed that the valence bands of BMO, CNO and

CN are situated at energy levels of 2.13, 1.72 and 1.51 eV, respectively. These findings suggest that Bi_2MoO_6 exhibits thermodynamic favorability towards nitrogen oxidation for nitrate generation [49]. According to the band gap position, the conventional type II or S-type heterojunction might construct in the system. Based on the next experimental findings, BMO, BBC and BCO-3 demonstrated notable photocatalytic capability in oxidizing nitrogen to produce nitrate. Conversely, CNO exhibited minimal activity in this regard. These outcomes are consistent with the S-scheme mechanism.

The piezoelectric properties of the samples prepared were evaluated using piezoresponse force microscopy (PFM) measurements (Fig. S9, SI). The morphology image of BCO-3 in Fig. 3a and S9 (SI) exhibits a high degree of similarity to both the corresponding piezo-response amplitude (Fig. 3b) and phase images (Fig. 3c), indicating that BCO-3 demonstrates exceptional performance in terms of its piezoelectric response. Furthermore, BMO, CNO, BBC and BCO-3 exhibited a typical amplitude-voltage butterfly curve (Fig. 3d and S10a-d, SI) and displayed a distinct hysteresis of 180° phase change (Fig. 3e and S10e-h, SI) when subjected to a reversal field of 10 V. This observation confirms the inherent piezoelectric properties of these materials. By analyzing the amplitude-
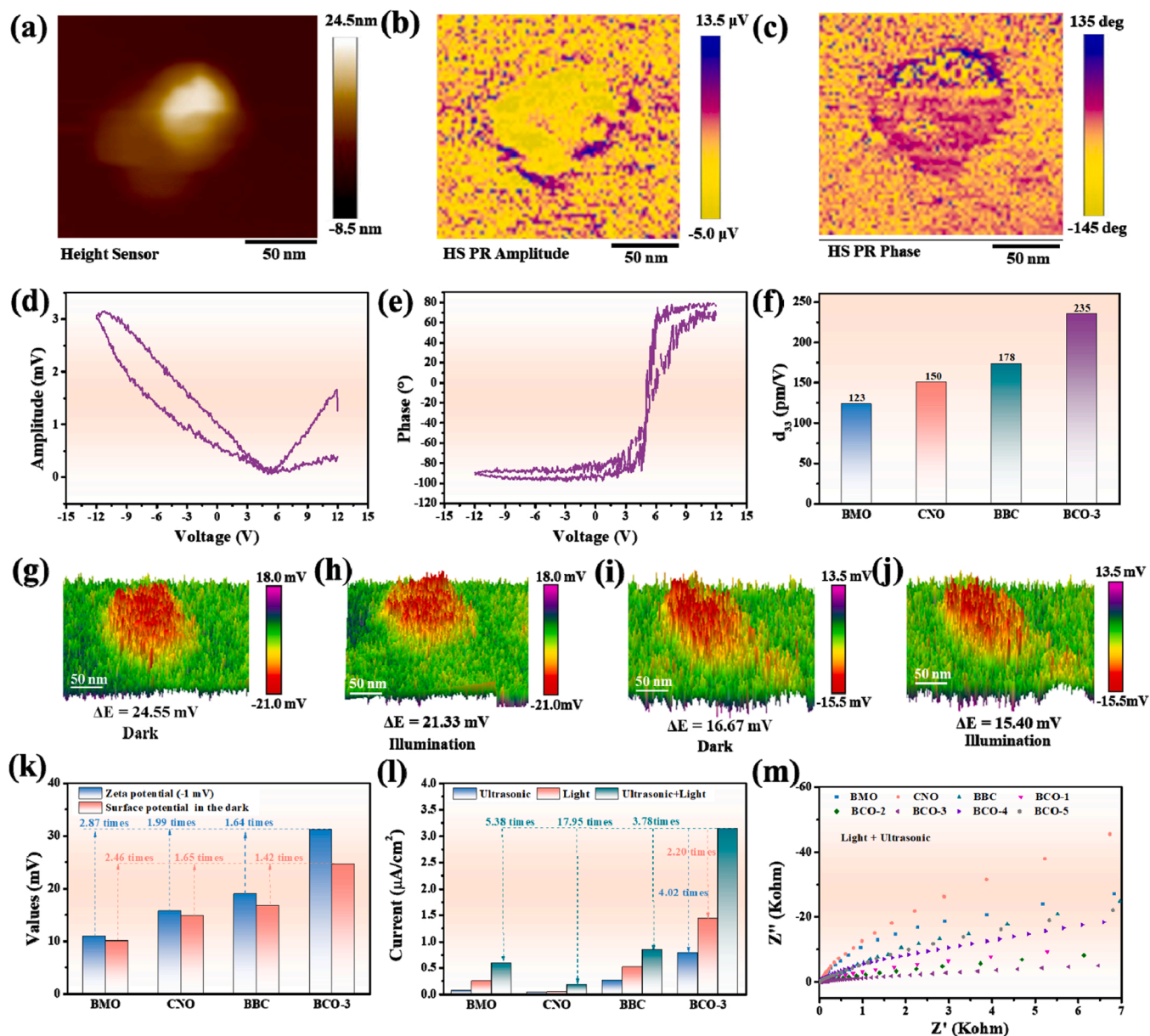
Fig. 3. PFM image of BCO-3 (a) Topography image, (b) amplitude image (c) phase image. (d) Piezoresponse amplitude butterfly loops and (e) phase hysteresis loops of BCO-3. (f) The maximum effective piezoelectric coefficient of the prepared samples. KPFM potential images of BCO-3: (g) in the dark and (h) under illumination. BBC: (i) in the dark and (j) under illumination. (k) The corresponding surface potential in the dark and Zeta potential of as prepared samples. (l) Current density responses of as prepared samples under different conditions. (m) Impedance comparison of as prepared samples under different conditions.

voltage butterfly loops, it was determined that the d_{33} values for BMO, CNO, BBC and BCO-3 are measured at 123, 150, 178 and 235 pm V^{-1} (Fig. 3f), respectively. As we known, the distinctive asymmetrical layered structures along with the presence of oxygen vacancies can give rise to a substantial intrinsic dipole moment [50,51]. On the other hand, carboxyl groups also provide polar groups in the CNO. Due to the Bi-COOH bond interaction, the notably higher piezoelectric response can be observed in BCO-3 as compared to BBC. Therefore, it can be concluded that the Bi-COOH bond interaction induce a polarity interaction for causing a large intrinsic piezoelectricity.

Encouraged by the piezoelectric and optical properties, the piezo-photocatalytic effect is worth to anticipate. To obtain a thorough understanding of the synergistic piezo-photocatalytic process, KPFM is utilized for surface potential measurement under both dark and illuminated circumstances. As manifested in Fig. 3g–j and Fig. S11 (SI), the surface potential of BCO-3 (24.55 mV) in the dark is higher than that of

BMO, CNO and BBC, which suggests a highest level of inherent polarization in the crystal structure of BCO-3. A significant polarization enhances the ability of BCO-3 nanosheets to generate high levels of piezoelectricity, which in turn promotes the creation of a desirable built-in piezoelectric field (Fig. 3k, S12 and table S1, SI) [52]. Interestingly, the surface potential of BCO-3 in the dark decreased to 21.33 mV after light irradiation, which can be explained by the piezo-generated polarization charge partially reduced the photo-induced charges [53]. In addition, the reduced surface potential in BCO-3 is larger than that of BMO, CNO and BBC, suggesting the Bi-COOH induce the built-in electric field for enhancing carrier transfer.

To verify the enhanced charge carrier transport properties, a sequence of measurements was carried out. For photocatalysis, excitonic effects greatly limited the polymer charge transport properties and can be analyzed by steady-stead fluorescence spectra [54]. As presented in Fig. S13 (SI), the lowest fluorescence intensity in BCO-3 proved the

notably reduced population of singlet excitons. Moreover, the temperature-dependent photoluminescence (TD-PL) is an effective characterization for observing exciton dissociation performance. As displayed in Fig. S14 (SI), the exciton dissociation energy is calculated as 102, 139, 161 and 445 meV for BCO-3, BBC, BMO, CNO, respectively, suggesting the existence of Bi-COOH in the S-scheme heterojunction can dissociate more exciton to free charges. To reveal the real charge transfer behavior, the current responses under different condition were carried out. As exhibited in Fig. 3l and S15 (SI), BCO-3 exists the highest photocurrent density compared with Bi_2MoO_6, BBC and CNO, implying enhanced charge separation and transfer in a polar S-scheme heterojunction. In addition, the BCO-3 also exhibited higher piezoelectric current, suggesting the polar unites easier to induce piezoelectric current. Notably, BCO-3 has the higher current density and smaller resistance under visible light irritation and ultrasonic vibration (Fig. 3m and S15-S16, SI), which is 2.20 and 4.02 times that of under light irritation or ultrasonic vibration, suggesting the polarity interaction is conduced to the charge transfer.

To reveal the intrinsic synergies, the calculation using the density functional theory (DFT) has been conducted. As shown in Fig. S17 (SI), the VB of BCO is mainly consist of Bi p, Mo d and O p orbitals, and the CB are contributed to the O p and N p orbitals. Furthermore, the Bi p orbitals was closer to the Fermi level in compress state, suggesting the Bi-COOH facilitates to stress response and generate more electron-hole pairs to improve the efficiency of charge transfer. In addition, the work function of BMO, CN and CNO are 2.308, 5.715 and 4.569 eV, suggesting the internal current are transfer from the BMO to CNO or CN (Fig. S18, SI), which is conform to the S-scheme mechanism. Furthermore, the proximity of the Fermi level between CNO and BMO facilitates efficient carrier transport across the heterojunction by incorporating COOH. Interestingly, the introduction of mechanical strain resulted in a significant reduction in the work function of BMO towards CNO or CN. This implies that the energy required to excite electrons to attain the vacuum state is diminished, thereby augmenting charge transfer on the catalyst's surface and ultimately enhancing the rate of catalytic reactions. In order to further reveal the intrinsic charge distribution, the differential charge density is calculated. As displayed in Fig. S19 (SI), the homogeneous charge accumulation and charge loss in various materials is observed for BBC. However, the charge accumulation on the Bi–O is transferred to CNO via the Bi-COOH, which acts as an electronic channel and enhances the smooth transfer of photoinduced charges (Fig. S20, SI). The findings also suggest that the presence of Bi-COOH bonds induces polarity interaction, resulting in an enhanced dipole moment, which is harmony with the P–E loops results (Fig. S21, SI). This enhancement proves advantageous for achieving a more favorable piezo-catalytic performance. Notably, those phenomena are more pronounced under compressive stress, indicating that stress enhances the interaction of polarities and resulted in the enchantment of charge transfer. Therefore, it can be concluded that the presence of Bi-COOH bonds not only induces polarity interaction for enhancing dipole moment, but also acts as an electronic channel to promote the charge transfer.

3.3. Piezo-photocatalytic activity

In this particular system, the production efficiency of HNO_3 is achieved through the direct oxidation of nitrogen using oxygen and water. Based on the conducted experiment, both materials and oxygen as an oxidizing agent are deemed essential. As exhibited in Fig. 4a–b and Fig. S22 (SI), the photocatalytic formation rate of HNO_3 for BMO, BBC, BCO-1, BCO-2, BCO-3, BCO-4 and BCO-5 are 0.574, 1.045, 2.071, 2.590, 3.339, 1.951 and 1.664 mg g^{-1} h^{-1}. Notably, BCO-3 demonstrated
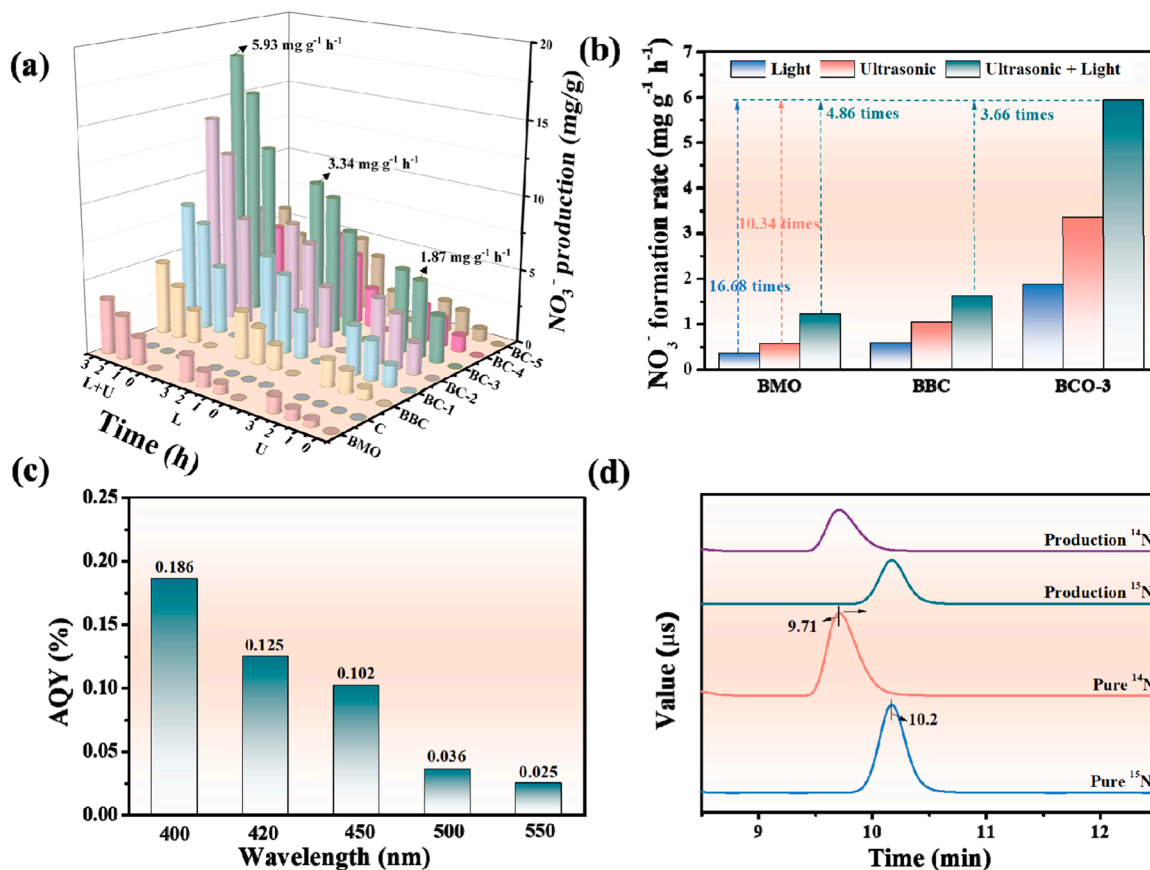

Fig. 4. (a) Photocatalytic NO_3^- yields over as-prepared samples under different conditions. (b) The NO_3^- formation rates under different conditions. (c) The apparent quantum efficiency of BCO-3. (d) ^{15}N isotope tracing results over BCO-3.

remarkable performance, surpassing BMO and BBC by factors of 5.82 and 3.20, respectively, while also outperforming previously reported studies (Table S2). That occurrence could be ascribed to the remarkable electrical transfer capacity exhibited throughout the process of photocatalysis. Moreover, the quantum efficiency of BCO-3 at 400 nm could reach up to 0.186% (Fig. 4c and Table S3), and falls as the light absorption. In the piezocatalysis process, BCO-3 exhibited the strongest piezocatalytic HNO_3 production rate, which is belong to the largest piezoresponse induced massive piezoelectric current. For photopiezocatalysis process, the HNO_3 formation rate of BMO, BBC, BCO-1, BCO-2, BCO-3, BCO-4 and BCO-5 are 1.221, 1.619, 2.754, 4.598, 5.933, 2.115 and 1.951 mg g^{-1} h^{-1}. Obviously, BCO-3 have the best piezo-photocatalytic efficiency, which is 3.17 and 1.78 times than that of piezocatalytic and photocatalytic performance, suggesting the enhanced polarization electric field in BCO-3 boosted the carrier separation and the directional migration of the carriers. To confirm high selectivity of the product, no other by-product can be

observed in the ^{1}HNMR, gas chromatography, ion chromatography, suggesting the only product was HNO_3 in this system (Fig. S23, SI). On the other hand, we use the isotope experiment to confirm the origin of the generated HNO_3. Obviously, HNO_3 in this system is solely derived from the oxidation of N_2 (Fig. 4d). The reusability of the catalyst was evaluated via cycling reaction and the characterization of the used catalyst. As shown in Fig. S24 (SI), the piezocatalytic, photocatalytic and piezo-photocatalytic performance in the BCO-3 exhibited a slight decline after ten runs. Additionally, the XRD, XPS, and FT-IR data along with SEM images revealed subtle alterations in the primary structure, which can be attributed to a decrease in the long-term operation of oxygen vacancies (Fig. S25-S26, SI). However, the catalyst retains 90% of its initial activity, demonstrating suggesting the high stability of BCO-3. Above all, BCO-3 could act as a good candidate for the direct oxidation of nitrogen with oxygen and water to produce HNO_3.

3.4. Mechanism of N_2 fixation

The direct oxidation of nitrogen with oxygen and water to produce HNO_3 involved multiple reactants (N_2, O_2 and H_2O). To explore its surface properties, the water contact angle, N_2 and O_2 temperature

programmed desorption (TPD) were carried out. As shown in Fig. S27 (SI), all the prepared samples have the nature of the hydrophilic properties. Moreover, the water contact angle of the BCO-3 is the smaller than that of BBC, CNO and BMO. The N_2 and O_2-TPD results also confirmed that BCO have outstanding N_2 and O_2 adsorption performance (Fig. S28, SI), suggesting the Bi-COOH is beneficial for reactant activation. To reveal the reactive radical, the free radical trapping experiment were implemented. As exhibited in Fig. S29 (SI), the near-inactivation performance can be seen by adding the superoxide radical trapping agent, suggesting the superoxide radical as a key active species.

Further, the nitrogen oxidation was deeply investigated through *in situ* FT-IR instrument. As shown in Fig. 5a, the peak at 930 cm^{-1} is the characteristic peaks of O_2^{-}, which is harmony with the radical trapping results. Moreover, the peaks at 1125 and 1623 cm^{-1} belongs to the characteristic peaks of $*N_2O_2$ [55,56]. The band at 1555 cm^{-1} are assigned to the NO stretching mode [57,58]. In addition, other peaks can be vested in the different adsorption states of NO_3 [59,60]. Those results suggested that the generation of HNO_3 undergo O_2^{-} and NO pathway. Therefore, the process of direct oxidation of nitrogen with oxygen and water to produce HNO_3 can be described as follow: $*O_2 \rightarrow *O_2^{-} \rightarrow *NO \rightarrow *HNO_3$.

To in-depth understanding the piezo-photocatalytic nitrogen oxidation process, the *in situ* Raman have been carried out. As shown in Fig. 5b, the vibration peaks generated by Bi−O are red-shifted under light and pressure, which proves that the stretching of the bond length leads to internal reconstruction, and leads to the activated nitrogen molecule, which is harmony with the DFT results (Fig. 30, SI). This outcome can be attributed to the presence of shortened Bi-COOH bonds, which led to the stretching of surface Bi−O and consequently resulted in both charge heterogeneity and activation of surface molecules. On the contrary, the BCO exhibits a higher charge difference and bond length difference between two adsorbed N≡N bonds compared to BBC (Fig. 5c–e). This indicates that the surface reconstructed structure reinforced the polarization of N_2 and electron transfer, thereby facilitating the fracture of the N≡N bonds. Additionally, under conditions of less than 100 MPa, the BCO exhibits more pronounced local polarization and fracture of N≡N bonds, suggesting that ultrasound-induced accelerated internal reconstruction leads to localized polarization and charge
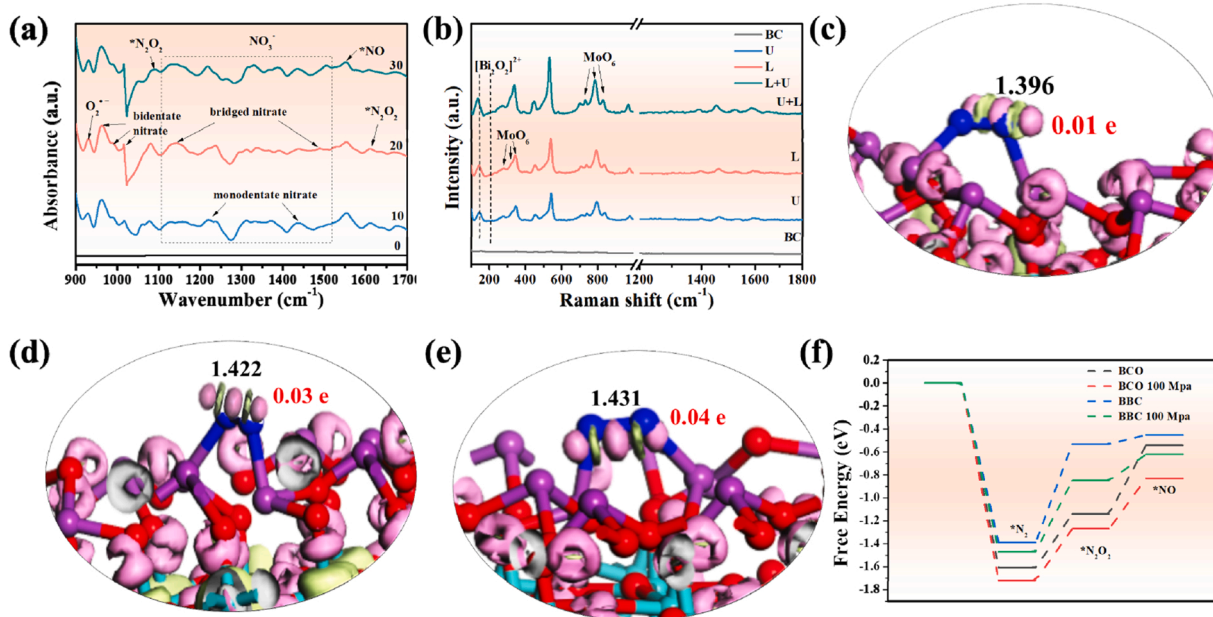

Fig. 5. (a) *In situ* FT-IR spectra and (b) *in-situ* Raman spectrum for catalytic nitrogen oxidation to nitric acid over BCO-3. Differential charge distribution of absorbed O_2 over (c) BBC under no stress, (d) BCO under no stress and (e) BCO under 100 MPa. (f) Gibbs free energy for the nitrogen oxidation to nitric acid progress over the prepared samples.

exchange of N≡N bonds.

Gibbs free energy calculations offer valuable insights into the characteristics of this process's reaction. As exhibited in Fig. 5f and S31-S32 (SI), BCO has the lowest activation energy for the nitrogen oxidation under different conditions, which is Bi-COOH induced internal reconstruction and results in the reduce reaction activation energy. Significantly, the $*N_2O_2$ intermediate is formed through the superoxide radical's further activation of N_2, which presents a significant energy barrier for the reaction due to the huge energy barrier. Clearly, the mechanical energy plays a significant role in promoting the initial activation of $*N_2O_2$ through a reduction in free energy of 0.45 eV, indicating the piezoelectric action enhanced polar coupling and results in the reinforcement of superoxide free radicals' attack. Considering the aforementioned findings, a comprehensive understanding of the operational principles behind BCO-3 can be achieved. At the beginning, both Bi_2MoO_6 and C_3N_4 could generated charge under light and ultrasonic condition. Due to the polarity interaction of BCO, Bi-COOH bonds establish a carrier migration channel that promotes charge transfer. Consequently, electrons on the surface of CNO react with O_2 to generate superoxide radicals. These radicals can then attack N_2 in conjunction with holes on the BMO, resulting in the formation of NO and ultimately leading to HNO_3 production.

4. Conclusion

In summary, the carboxylated C_3N_4 and Bi_2MoO_6 S-scheme heterostructure were successfully synthesized via a facile hydrothermal method for efficient piezo-photocatalytic N_2 oxidation to generate NO_3. The optimal carboxylated C_3N_4-Bi_2MoO_6 catalyst revealed outstanding nitric acid production rates of 5930 µg g^{-1} h^{-1} under the stimulation of ultrasonication and light illumination. The experimental and DFT results show that the interaction of Bi-COOH between Bi_2MoO_6 and g-C_3N_4 induce polarity interaction and structural reconstruction. The polarity interaction facilitates the acceleration of charge distribution and serves as a pathway for carrier migration, thereby enhancing charge transfer and dipole moment. Additionally, the interaction of polarity and structural reconstruction reinforces N_2 polarization and electron transfer, ultimately facilitating the cleavage of N≡N bonds and reducing reaction activation energy. Significantly, the utilization of the piezoelectric effect has the potential to enhance charge separation efficiency and decrease the energy required for nitrogen oxidation. The present study introduces a novel methodology to achieve efficiently converting N_2 into clean nitric acid.

CRediT authorship contribution statement

Xiaoxu Deng: Writing – original draft, Formal analysis, Data curation, Conceptualization. **Peng Chen**: Writing – review & editing, Supervision, Funding acquisition, Data curation. **Ruirui Cui**: Formal analysis, Conceptualization. **Xingyong Gong**: Investigation, Formal analysis. **Xucheng Li**: Formal analysis, Data curation. **Xu Wang**: Supervision, Software, Funding acquisition. **Chaoyong Deng**: Supervision, Formal analysis, Data curation.

Declaration of Competing Interest

The authors declare that they have no known competing financial interests or personal relationships that could have appeared to influence the work reported in this paper.

Data Availability

Data will be made available on request.

Appendix A. Supporting information

Supplementary data associated with this article can be found in the online version at doi:10.1016/j.apcatb.2024.123977.

References

[1] T. Li, S. Han, Y. Wang, J. Zhou, B. Zhang, Y. Yu, A spectroscopic study on nitrogen electrooxidation to nitrate, Angew. Chem. Int. Ed. 62 (2023) e202217411.

[2] S. Han, C. Wang, Y. Wang, Y. Yu, B. Zhang, Electrosynthesis of nitrate via the oxidation of nitrogen on tensile-strained palladium porous nanosheets, Angew. Chem. Int. Ed. 60 (2021) 4474.

[3] M. Kuang, Y. Wang, W. Fang, H. Tan, M. Chen, J. Yao, C. Liu, J. Xu, K. Zhou, Q. Yan, Efficient nitrate synthesis via ambient nitrogen oxidation with Ru-doped TiO$_2$/RuO$_2$ electrocatalysts, Adv. Mater. 32 (2020) 2002189.

[4] J.G. Chen, R.M. Crooks, L.C. Seefeldt, K.L. Bren, R.M. Bullock, M.Y. Darensbourg, P.L. Holland, B. Hoffman, M.J. Janik, A.K. Jones, M.G. Kanatzidis, P. King, K. M. Lancaster, S.V. Lymar, P. Pfromm, W.F. Schneider, R.R. Schrock, Beyond fossil fuel-driven nitrogen transformations, Science 360 (2018) eaar6611.

[5] H. Wan, A. Bagger, J. Rossmeisl, Limitations of electrochemical nitrogen oxidation toward nitrate, J. Phys. Chem. Lett. 13 (2022) 8928.

[6] J. Yang, Z. Ruan, S. Jiang, P. Xia, Q. Yang, Q. Zhang, C. Xiao, Y. Xie, Ce-doped W$_{18}$O$_{49}$ nanowires for tuning N$_2$ activation toward direct nitrate photosynthesis, J. Phys. Chem. Lett. 12 (2021) 11295.

[7] Y. Zhang, F. Du, R. Wang, X. Ling, X. Wang, Q. Shen, Y. Xiong, T. Li, Y. Zhou, Z. Zou, Electrocatalytic fixation of N$_2$ into NO$_3$: electron transfer between oxygen vacancies and loaded Au in Nb$_2$O$_{5-x}$ nanobelts to promote ambient nitrogen oxidation, J. Mater. Chem. A 9 (2021) 17442–17450.

[8] Y. Liu, M. Cheng, Z. He, B. Gu, C. Xiao, T. Zhou, Z. Guo, J. Liu, H. He, B. Ye, B. Pan, Y. Xie, Pothole-rich ultrathin WO$_3$ nanosheets that trigger N≡N bond activation of nitrogen for direct nitrate photosynthesis, Angew. Chem. Int. Ed. 58 (2019) 731.

[9] P. Xia, X. Pan, S. Jiang, J. Yu, B. He, P. Ismail, W. Bai, J. Yang, L. Yang, H. Zhang, M. Cheng, H. Li, Q. Zhang, C. Xiao, Y. Xie, Designing a redox heterojunction for photocatalytic "overall nitrogen fixation" under mild conditions, Adv. Mater. 34 (2022) 2200563.

[10] M. Song, S. Yang, H. Peng, T. Zhao, F. Liu, P. Chen, S. Yin, Linkage engineered the donor–acceptor motifs of poly (heptazine imide) for enhancing the piezo-photocatalytic nitrogen fixation, Nano Energy 116 (2023) 108784.

[11] X. Deng, P. Chen, R. Cui, W. Huang, Y. Wu, X. Wang, C. Deng, Tip effect and structural disordering in Bi$_2$WO$_6$ for enhanced piezo-photocatalytic nitrogen oxidation to nitric acid, Appl. Catal. B: Environ. 339 (2023) 123148.

[12] R. Tang, D. Gong, Y. Zhou, Y. Deng, C. Feng, S. Xiong, Y. Huang, G. Peng, L. Li, Unique g-C$_3$N$_4$/PDI-g-C$_3$N$_4$ homojunction with synergistic piezo-photocatalytic effect for aquatic contaminant control and H$_2$O$_2$ generation under visible light, Appl. Catal. B: Environ. 303 (2022) 120929.

[13] W. Tian, N. Li, D. Chen, Q. Xu, H. Li, C. Yan, J. Lu, Vibration-driven reduction of CO$_2$ to acetate with 100% selectivity by SnS nanobelt piezocatalysts, Angew. Chem. Int. Ed. 62 (2023) e202306964.

[14] Y. Dong, S. Dong, B. Liu, C. Yu, J. Liu, D. Yang, P. Yang, J. Lin, 2D piezoelectric Bi$_2$MoO$_6$ nanoribbons for GSH-enhanced sonodynamic therapy, Adv. Mater. 33 (2021) 2106838.

[15] S. Ji, H. Lei, M. Wu, Q. He, P. Sun, X. Dong, Piezoelectric polarization promoted spatial separation of photogenerated charges in Bi$_2$MoO$_6$ catalyst and investigation of its synergistic photopiezocatalytic activity, J. Taiwan Inst. Chem. Eng. 133 (2022) 104260.

[16] E. Gómez, R. Cestaro, L. Philippe, A. Serrà, Electrodeposition of nanostructured Bi$_2$MoO$_6$@Bi$_2$MoO$_{6-x}$ homojunction films for the enhanced visible-light-driven photocatalytic degradation of antibiotics, Appl. Catal. B: Environ. 317 (2022) 121703.

[17] T. Ma, C. Yang, L. Guo, R.A. Soomro, D. Wang, B. Xu, F. Fu, Refining electronic properties of Bi$_2$MoO$_6$ by In-doping for boosting overall nitrogen fixation via relay catalysis, Appl. Catal. B: Environ. 330 (2023) 122643.

[18] Q. Pan, J. Wang, H. Chen, P. Yin, Q. Cheng, Z. Xiao, Y.Z. Zhao, H.B. Liu, Piezo-photocatalysis of Sr-doped Bi$_4$O$_5$Br$_2$/Bi$_2$MoO$_6$ composite nanofibers to simultaneously remove inorganic and organic contaminants, J. Water Process Eng. 56 (2023) 104330.

[19] Y. Wu, D. Yang, Y. Zhang, S. Jiao, W. Tang, Z. Wang, N. Wu, Y. Wang, W. Zhong, A. Zhang, J. Hao, H. Cai, X. Wu, Integrated unit-cell-thin MXene and Schottky electric field into piezo-photocatalyst for enhanced photocarrier separation and hydrogen evolution, Chem. Eng. J. 439 (2022) 135640.

[20] C. Hu, F. Chen, Y. Wang, N. Tian, T. Ma, Y. Zhang, H. Huang, Exceptional cocatalyst-free photo-enhanced piezocatalytic hydrogen evolution of carbon nitride nanosheets from strong in-plane polarization, Adv. Mater. 33 (2021) 2101751.

[21] Q. Zhao, Z. Liu, Z. Guo, M. Ruan, W. Yan, The collaborative mechanism of surface S-vacancies and piezoelectric polarization for boosting CdS photoelectrochemical performance, Chem. Eng. J. 433 (2022) 133226.

[22] P. Hu, Y. Xu, Y. Lei, J. Yuan, R. Lei, R. Hu, J. Chen, D. Xu, S. Zhang, P. Liu, X. Zhang, X. Qiu, W. Feng, Piezoelectric nanofoams with the interlaced ultrathin graphene confining Zn–N–C dipoles for efficient piezocatalytic H_2 evolution under low-frequency vibration, J. Energy Chem. 69 (2022) 115.

[23] W. Dai, J. Long, L. Yang, S. Zhang, Y. Xu, X. Luo, J. Zou, S. Luo, Oxygen migration triggering molybdenum exposure in oxygen vacancy-rich ultra-thin Bi_2MoO_6 nanoflakes: dual binding sites governing selective CO_2 reduction into liquid hydrocarbons, J. Energy Chem. 61 (2021) 281.

[24] M. Xu, M. Lu, G. Qin, X. Wu, T. Yu, L. Zhang, K. Li, X. Cheng, Y. Lan, Piezo-photocatalytic synergy in $BiFeO_3$@COF Z-scheme heterostructures for high-efficiency overall water splitting, Angew. Chem. Int. Ed. 61 (2022) e202210700.

[25] L. Sun, X. Yu, L. Tang, W. Wang, Q. Liu, Hollow dodecahedron $K_3PW_{12}O_{40}$/CdS core-shell S-scheme heterojunction for photocatalytic synergistic H_2 evolution and benzyl alcohol oxidation, Chin. J. Catal. 52 (2023) 164–175.

[26] W. Wang, S. Mei, H. Jiang, L. Wang, H. Tang, Q. Liu, Recent advances in TiO_2-based S-scheme heterojunction photocatalysts, Chin. J. Catal. 55 (2023) 137–158.

[27] L. Wang, T. Yang, L. Peng, Q. Zhang, X. She, H. Tang, Q. Liu, Dual transfer channels of photo-carriers in 2D/2D/2D sandwich-like $ZnIn_2S_4$/g-C_3N_4/Ti_3C_2 MXene S-scheme/Schottky heterojunction for boosting photocatalytic H_2 evolution, Chin. J. Catal. 43 (2022) 2720–2731.

[28] B. Zhu, X. Hong, L. Tang, Q. Liu, H. Tang, Enhanced photocatalytic CO_2 reduction over 2D/1D $BiOBr_{0.5}Cl_{0.5}$/WO_3 S-Scheme heterostructure, Acta Phys. -Chim. Sin. 38 (2022) 2111008.

[29] P. Wang, S. Fan, X. Li, J. Duan, D. Zhang, Modulating the molecular structure of graphitic carbon nitride for identifying the impact of the piezoelectric effect on photocatalytic H_2O_2 production, ACS Catal. 13 (2023) 9515.

[30] Q. Zeng, Z. Jia, X. Liu, B. Xiu, J. Cheng, Multi-interface polarization engineering constructed ^1T–^2H MoS_2 QDs/Y-$NaBi(MoO_4)_2$ multiple heterostructure for high-efficient piezoelectric-photoelectrocatalysis PDE-5i degradation, Appl. Catal. B: Environ. 327 (2023) 122460.

[31] K. Chu, Q.Q. Li, Y.P. Liu, J. Wang, Y.H. Cheng, Filling the nitrogen vacancies with sulphur dopants in graphitic C_3N_4 for efficient and robust electrocatalytic nitrogen reduction, Appl. Catal. B: Environ. 267 (2020) 118693.

[32] J. Yang, T. Xie, Y. Mei, J. Chen, H. Sun, S. Feng, Y. Zhang, Y. Zhao, J. Wang, X. Li, J. He, H. Chen, High-efficiency V-mediated Bi_2MoO_6 photocatalyst for PMS activation: modulation of energy band structure and enhancement of surface reaction, Appl. Catal. B: Environ. 339 (2023) 123149.

[33] Y. Tian, F. Cheng, X. Zhang, F. Yan, B. Zhou, Z. Chen, J. Liu, F. Xi, X. Dong, Solvothermal synthesis and enhanced visible light photocatalytic activity of novel graphitic carbon nitride-Bi_2MoO_6 heterojunctions, Powder Technol. 267 (2014) 126.

[34] N. He, Z. Guo, C. Zhang, Y. Yu, L. Tan, H. Luo, L. Li, J. Bahnemann, H. Chen, F. Jiang, Bifunctional 2D/2D g-C_3N_4/BiO_{2-x} nanosheets heterojunction for bacterial disinfection mechanisms under visible and near-infrared light irradiation, J. Hazard. Mater. 436 (2022) 129123.

[35] D. Yao, C. Tang, A. Vasileff, X. Zhi, Y. Jiao, S.Z. Qiao, The controllable reconstruction of Bi-MOFs for electrochemical CO_2 reduction through electrolyte and potential mediation, Angew. Chem. Int. Ed. 60 (2021) 18178.

[36] Y. Deng, J. Wang, J. Wang, H. Zhang, H. Xiao, C. Zhang, W. Wang, In situ growth of Bi/Ag double quantum dots on hollow Bi_2MoO_6 microspheres: enhancement of the surface plasmon resonance effect on PMS activation, Appl. Catal. B: Environ. 338 (2023) 123041.

[37] L. Zhang, Z. Wang, C. Hu, B. Shi, Enhanced photocatalytic performance by the synergy of Bi vacancies and Bi^0 in Bi^0-$Bi_{2-δ}MoO_6$, Appl. Catal. B: Environ. 257 (2019) 117785.

[38] S. Khatun, K. Shimizu, S. Singha, R. Saha, S. Watanabe, P. Roy, Defect enriched hierarchical iron promoted Bi_2MoO_6 hollow spheres as efficient electrocatalyst for water oxidation, Chem. Eng. J. 426 (2021) 131884.

[39] Z. Huang, S. Zhao, Y. Yu, Experimental method to explore the adaptation degree of type-II and all-solid-state Z-scheme heterojunction structures in the same degradation system, Chin. J. Catal. 41 (2020) 1522.

[40] Q. Wang, X. Deng, H. Pen, F. Liu, M. Song, P. Chen, S.F. Yin, Insights into the synergistic promotion of spin polarization over $C_3N_{5.4}$ for enhancing cooperative hydrogen evolution and benzylamine oxidation coupling, Nano Res. 16 (2022) 4225–4232.

[41] J. He, Z. Yang, Z. Wang, R. Fang, L. Gu, Y. Yan, J. Ran, Systematic study of H_2 production from photothermal reforming of α-cellulose over atomically thin Bi_2MoO_6, Energy Convers. Manag. 277 (2023) 116605.

[42] Z. Zhang, L. Cui, Y. Zhang, L.H. Klausen, M. Chen, D. Sun, S. Xu, S. Kang, J. Shi, Regulation of carboxyl groups and structural defects of graphitic carbon nitride via environmental-friendly glucose oxidase ring-opening modulation, Appl. Catal. B: Environ. 297 (2021) 120441.

[43] J. Di, X. Zhao, C. Lian, M. Ji, J. Xia, J. Xiong, W. Zhou, X. Cao, Y. She, H. Liu, K. P. Loh, S.J. Pennycook, H. Li, Z. Liu, Atomically-thin Bi_2MoO_6 nanosheets with vacancy pairs for improved photocatalytic CO_2 reduction, Nano Energy 61 (2019) 54.

[44] D. Li, T. Li, G. Hao, W. Guo, S. Chen, G. Liu, J. Li, Q. Zhao, IrO_2 nanoparticle-decorated single-layer NiFe LDHs nanosheets with oxygen vacancies for the oxygen evolution reaction, Chem. Eng. J. 399 (2020) 125738.

[45] X. Cao, A. Huang, C. Liang, H.C. Chen, T. Han, R. Lin, Q. Peng, Z. Zhuang, R. Shen, H.M. Chen, Y. Yu, C. Chen, Y. Li, Engineering lattice disorder on a photocatalyst: photochromic BiOBr nanosheets enhance activation of aromatic C-H bonds via water oxidation, J. Am. Chem. Soc. 144 (2022) 3386–3397.

[46] D.B. Kleja, J.P. Gustafsson, V. Kessler, I. Persson, Bismuth(III) forms exceptionally strong complexes with natural organic matter, Environ. Sci. Technol. 56 (2022) 3076–3084.

[47] B.V. Egorova, E.V. Matazova, G.Y. Aleshin, A.D. Zubenko, A.V. Pashanova, E. A. Konopkina, A.A. Mitrofanov, A.A. Smirnova, A.L. Trigub, V.A. Karnoukhova, O. A. Fedorova, S.N. Kalmykov, Investigating the bismuth complexes with benzoazacrown Tri- and Tetra-acetates, Eur. J. Inorg. Chem. 2021 (2021) 3344–3354.

[48] Y. Li, X. Zhang, R. Sha, T. Li, C. Hu, S. Tu, F. Chen, H. Huang, Efficient piezo-photocatalysis of $Bi_2O_2(OH)NO_3$/BiOI heterojunction: collaboration of piezoelectric polarization and interface electric field, Chem. Eng. J. 480 (2024) 147976.

[49] W. Ren, Z. Mei, S. Zheng, S. Li, F. Pan, Wavelength-dependent solar N_2 fixation into ammonia and nitrate in pure water, Research 2020 (2020) 3750314.

[50] Q. Tang, J. Wu, X.Z. Chen, R. Sanchis-Gual, A. Veciana, C. Franco, D. Kim, I. Surin, J. Pérez-Ramírez, M. Mattera, A. Terzopoulou, N. Qin, M. Vukomanovic, B. J. Nelson, J. Puigmartí-Luis, S. Pané, Tuning oxygen vacancies in $Bi_4Ti_3O_{12}$ nanosheets to boost piezo-photocatalytic activity, Nano Energy 108 (2023) 108202.

[51] T. Li, C. Hu, H. Li, Y. Zhang, H. Huang, Piezoelectric polarization and interfacial electric field synergistically promote piezo-photocatalysis of *in-situ* transformed heterojunction, Appl. Surf. Sci. 630 (2023) 157478.

[52] C. Wang, C. Hu, F. Chen, H. Li, Y. Zhang, T. Ma, H. Huang, Polar layered bismuth-rich oxyhalide piezoelectrics $Bi_4O_5X_2$ (X = Br, I): Efficient piezocatalytic pure water splitting and interlayer anion-dependent activity, Adv. Funct. Mater. 33 (2023) 2301144.

[53] X. Huang, R. Lei, J. Yuan, F. Gao, C. Jiang, W. Feng, J. Zhuang, P. Liu, Insight into the piezo-photo coupling effect of $PbTiO_3$/CdS composites for piezo-photocatalytic hydrogen production, Appl. Catal. B: Environ. 282 (2021) 119586.

[54] H. Wang, S. Jiang, S. Chen, X. Zhang, W. Shao, X. Sun, Z. Zhao, Q. Zhang, Y. Luo, Y. Xie, Insights into the excitonic processes in polymeric photocatalysts, Chem. Sci. 8 (2017) 4087.

[55] Y. Zhao, X. Li, X. Fan, H. Wang, Y. Liu, Y. Chen, T. Yang, J. Ye, H. Huang, H. Li, X. Zhang, Y. Liu, H. Lin, Z. Kang, Small-molecule catalyzed H_2O_2 production via a phase-transfer photocatalytic process, Appl. Catal. B: Environ. 314 (2022) 121499.

[56] J. Yang, L. Li, C. Xiao, Y. Xie, Dual-plasmon resonance coupling promoting directional photosynthesis of nitrate from air, Angew. Chem. Int. Ed. 62 (2023) e202311911.

[57] X. Zhang, R. Shi, Z. Li, J. Zhao, H. Huang, C. Zhou, T. Zhang, Photothermal-assisted photocatalytic nitrogen oxidation to nitric acid on palladium-decorated titanium oxide, Adv. Energy Mater. 12 (2022) 2103740.

[58] M. Guo, L. Fang, L. Zhang, M. Li, M. Cong, X. Guan, C. Shi, C. Gu, X. Liu, Y. Wang, X. Ding, Pulsed electrocatalysis enabling high overall nitrogen fixation performance for atomically dispersed Fe on TiO_2, Angew. Chem. Int. Ed. 62 (2023) e202217635.

[59] C. Dai, Y. Sun, G. Chen, A.C. Fisher, Z.J. Xu, Electrochemical oxidation of nitrogen towards direct nitrate production on spinel oxides, Angew. Chem. Int. Ed. 59 (2020) 9418.

[60] S. Zhang, Y. Zhao, Y. Miao, Y. Xu, J. Ran, Z. Wang, Y. Weng, T. Zhang, Understanding aerobic nitrogen photooxidation on titania through *in situ* time-resolved spectroscopy, Angew. Chem. Int. Ed. 61 (2022) e202211469.